Volume 15, Issue 2, 152514 (1-10)

Iranian Journal of Catalysis (IJC)

https://doi.org/10.57647/j.ijc.2025.1502.14

Synthesis of new $CuO/La_2CoFe_2O_7$ nanocomposite, and investigation of Its photocatalytic property in removing organic dye

Somaye Khammarnia*, Hassan Hassani

Department of Chemistry, Payame Noor University, Tehran, Iran.

***Corresponding author:** somayekhammarnia@pnu.ac.ir

Original Research

Received:
8 February 2025
Revised:
29 March 2025
Accepted:
26 April 2025
Published online:
3 May 2025

Abstract:

Some novel CuO (x)/$La_2CoFe_2O_7$ (x = 0 – 70%) nanocomposites were synthesized using the sol-gel method. The formation of CuO (x)/$La_2CoFe_2O_7$ (x = 0 – 70%) nanocomposites was verified via various methods such as XRD, SEM, TEM, FTIR, UV-VIS, VSM, and photoluminescence. A transmission electron microscope images show spherical particles such as $La_2CoFe_2O_7$ and CuO (60%)/LCoFO with average grain sizes of 30 and 20 nm, respectively. VSM images show that the coercivity and saturation magnetization of this sample are about 137.53 Oe and 95.284 emu/g. The photocatalytic activity of CuO/$La_2CoFe_2O_7$ (CuO/LCoFO) nanoparticles was investigated by photodegradation under UV light irradiation and under optimized conditions of dye concentration (1.5×10^{-3} M), pH (= 6), irradiation time (50 min), and catalyst dose (7.0 g/L). Nanocomposite 60% shows the highest photocatalytic activity compared to pure LCoFO nanocomposite and other photocatalysts. A non-toxic, cheap, and highly active CuO (60%)/LCoFO nanocomposite photocatalyst was proposed to remove Methyl green (MG) and Basic fuchsin (BF) dyes under UV light irradiation.

Keywords: Basic fuchsin; Methyl green; Nanocomposite; Photocatalysts

1. Introduction

In recent years, environmental pollution has caused many problems for people's health. Textile factories and paper industries discharge their polluted wastewater into running water, which causes severe water pollution. The removal of toxic chemicals from an ecological and physiological perspective is an important issue in pollution control.
The removal of organic pollutants from the waters is considered to be of utmost importance since they are carcinogenic and toxic [1–4]. Textile wastewater contains many substances and pigments that pollute groundwater and surface water [5]. In the textile industry, the resulting effluent contains many colored compounds, such as the toxic compounds of Azomi dyes, which cause health problems and risks for the environment. Hence, organic dyes, even in low concentrations, can threaten the lives of people and the environment; therefore, the wastewater of these industries must be treated. There are various methods to remove dyes from the effluents of these industries [1, 6]. A suitable method for wastewater treatment in the presence of semiconductor materials is photocatalytic activity, and this is a practical method for the treatment of organic pollutants Therefore, according to recent research, photocatalytic decomposition is very effective in water and wastewater treatment technology [7, 8]. A number of semiconductor photocatalysts such as metal oxides TiO_2, WO_3, SnO_2, CeO_2, ZnO, Bi_2O_3, photocatalysts based on Ag, Nb_2O_5 were used to remove organic pollutants using UV light sources [9]. Semiconductor photocatalysts such as titanium dioxide (TiO_2) have been used in the photocatalytic degradation of organic pollutants due to their characteristics such as high effectiveness, stability, cost-effectiveness, and non-toxicity [10–12]. In this reaction, a semiconductor material is irradiated with suitable photons, usually in the UV and visible regions of light, and the electron and hole (e^-/h^+) pairs can be induced in the conduction band (CB) and valence band (VB) of the semiconductor, respectively. The e^-/h^+ pairs can participate in the degradation of the target pollutant in both direct and indirect ways. The photo-induced electrons are strong

reducing agents that can reduce the pollutant through the following processes. On the other hand, photogenerated holes are strong oxidizing agents that can directly attack organic pollutants and oxidize them to initiate the degradation process. In the indirect method, photo-induced electrons can reduce dissolved oxygen to produce highly reactive superoxide radicals.

In contrast, light-induced holes can attack water molecules or hydroxyl anions to produce hydroxyl radicals, which are strong oxidizing agents. These powerful radicals can effectively attack organic molecules and break them down into smaller intermediates. Ultimately, water, carbon dioxide, and other inorganic species are produced [13]. However, due to some problems such as rapid recombination of electrons and holes produced by photo and low efficiency for using solar light, the use of TiO_2 has decreased. LCoFO is one of the main materials of perovskite, it is used for many applications such as catalysts and magnetic materials. Recently, due to its good photocatalytic performance, it has been used in the decomposition of industrial dyes MV, MG, and EBT [14].To increase the photocatalytic performance of perovskite, methods such as metal and non-metal doping, increasing the surface by creating pores, and coupling with some semiconducting metal oxides are used [15–18]. The coupling method is more efficient than all these techniques, and there are examples of this coupling, such as the Ag_3PO_4-$LaFeO_3$ and Bi_2O_3/$BaTiO_3$ perovskite composites, which had better photocatalytic activity (PCA) than their isolated compounds [19]. Considering the special properties of copper oxide, such as semiconducting, non-toxic, and not rare, it is an available and inexpensive oxide that has received attention [20].

In the present work, CuO (x)/LCoFO nanocomposites (x $= 0-70\%$) were synthesized and identified by different structural and morphological methods, and their PCA was investigated under UV radiation, and among these samples, CuO (60%)/LCoFO has the highest PCA. Therefore, in this project, new inexpensive, strong, and magnetic photocatalysts were synthesized that can easily destroy pollutants under UV light. Eventually, the nanocomposite CuO (60%)/LCoFO non-toxic, cheap, very powerful, and stable photocatalyst is proposed as an effective photocatalyst for wastewater treatment.

2. Experimental

2.1 Required chemicals and equipment

$LaCl_3.\ 7H_2O$, Fe $(NO_3)_3.\ 9H_2O$, Co $(NO_3)_2.\ 6H_2O$, $CuCl_2.\ 6H_2O$, $C_8H_{16}O$, NaOH were bought from Merck Company. A Philips X-ray diffract meter with Ni-filtered CuKa radiation was employed for the study of Structural properties. TESCAN MIRA3 field emission scanning electron microscopy (FE-SEM) investigate the morphology of the generated NPs. Chemical bonds were analyzed by transmission infrared spectroscopy, using a Perkin Elmer 100 series spectrometer (FTIR). The ultraviolet-visible (UV-Vis) spectrum of the samples was studied by a Shimadzu UV-2450 spectrophotometer. TEM (Transmission electron microscope) images were taken by TEM (Zeiss—EM10C—100 kV). An alternating gradient force magnetometer (AGFM) device, made by Meghnatis Daghigh Kavir Co. (Kashan, Iran.) was used for the examination of room temperature magnetic properties in an applied magnetic field sweeping between $\pm 10,000$ Oe. A Perkin-ElmerLs55 photoluminescence spectrometer (PL) is employed to study the electrical, photoelectrical and optical attributes of nanocatalyst.

2.2 Synthesis of CuO/LCoFO nanocatalyst

New photocatalysts from nanocomposites CuO (x)/LCoFO (x $= 0-70\%$) were synthesized by the sol-gel method. To prepare nanocomposites CuO (x)/LCoFO (x $= 0-70\%$), stoichiometric values of LCoFO and CuO [21] were mixed together in a mortar for 30 minutes. Next, 80 mL of boiling distilled water was added to the prepared powder, and the prepared solution was ultrasonicated for one hour to make it uniform. The prepared solution was stirred at room temperature for 24 hours. Next, the obtained solution was heated for 12 hours at a temperature of 80 degrees Celsius to evaporate. Next, the prepared product was dried in the oven at a temperature of 80 °C for 8 hours. To produce CuO (x)/LCoFO composite, we calcined the powder for four hours at 400 °C.

2.3 Photocatalytic experiment

In this study, a certain amount of nanocatalyst (10 mg) was poured into 5 mL of MG and BF aqueous solutions (10^{-3} M) under magnetic stirring and dispersed separately. The suspension was exposed to UV radiation for 30 minutes. During the period of light irradiation, the effect of some parameters, such as solution pH, concentration of dyes, photocatalyst dose, irradiation time, and the percentage of CuO in the catalyst, was studied and optimized. Finally, reaction mixtures were centrifuged and filtered, and the residual concentrations of MG and BF were measured by UV–Vis spectrophotometer. Figure 1 shows the absorption of MG and BF residue by different doses of CuO (60%)/LCoFO nanocomposite.

3. Results and discussion

3.1 Nanocomposite characterization

The XRD pattern of pure LCoFO and CuO nanoparticles shown in figure 2 also shows CuO (x)LCoFO (x = 40, 60, 70)composites with different CuO content. The XRD pattern of $La_2CoFe_2O_7$ nanocomposite shows that it corresponds to the combination of $CoFe_2O_4$ and the standard (01-1121) and the diffraction with the highest intensity at $2\theta = 35.5$, and the combination of La_2O_3 and the standard (22-0641) with monoclinic symmetry and diffraction with The maximum intensity at $2\theta = 26.13$ corresponds perfectly. The structure of CuO conforms to the JCPDS pattern No. 05-0661. With the increase of CuO amount in the nanocomposites, peaks (shown by stars) appear in the XRD patterns and their intensity increases. It is deduced from this data formation that CuO/LCoFO composite. The average crystallite size of CuO, LcoFO, and the synthesized nanocomposites was obtained by the Williamson-Hall relationship and the Scherrer relationship. The Williamson-Hall

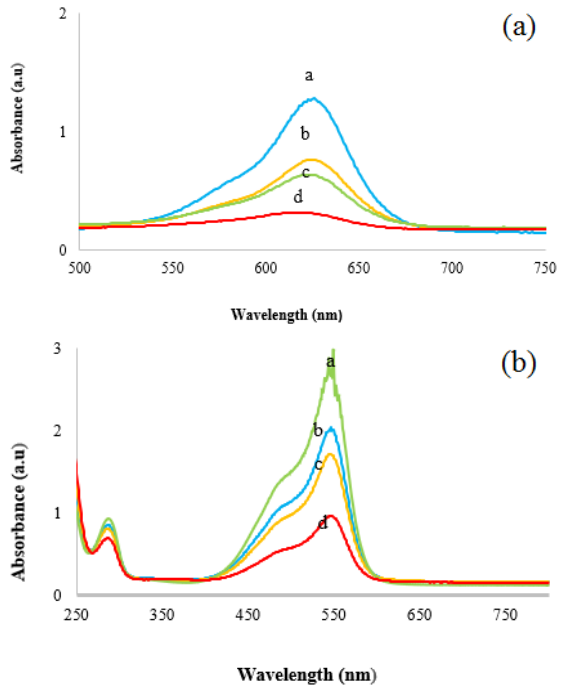

Figure 1. UV-Vis absorption spectra of FB (up) and MG (down) with (a) 0.0, (b) 1, (c) 3, and (d) 7 g/L CuO/$La_2CoFe_2O_7$ (CuO/LCoFO) nanoparticles.

relationship is shown in equation (1)

$$\beta_{\text{total}} \cos\theta = C_{\varepsilon W-H} \sin\theta + \frac{K\lambda}{D_{W-H}} \quad (1)$$

where D_{W-H} is the grain size determined from the Williamson-Hall diagram, K represents the shape factor, which has an approximate value of 0.9, λ is the wavelength of the X-ray source set in XRD, which is 0.154 nm. Comparing this equation with the standard equation for a straight line ($y = mx + c$), we see that by plotting $\beta_{\text{total}} \cos\theta$ versus $\sin\theta$, the strain component is obtained from the slope (C_ε) and the size component from the relationship $K\lambda/D_{W-H}$ [22]. The mean crystallite sizes for CuO, LCoFO, CuO (40%)/LcoFO, CuO (60%)/LcoFO, and CuO (70%)/LcoFO nanocomposites were found to be 96.25, 20, 49.65, 20.8, and 64.16 nm, respectively.

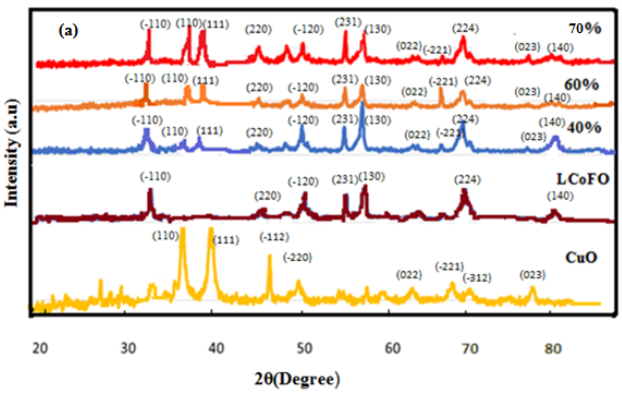

Figure 2. The XRD patterns of LCoFO, CuO and CuO (x)/LCoFO (x = 40, 60 and 70%) nanocomposites with various CuO content.

The Debye-Scherrer relationship is shown in equation (2)

$$D = \frac{K\chi}{\beta \cos\theta} \quad (2)$$

D denotes the average grain size, and K denotes the shape factor, which has a value of approximately. 0.9, k means the wavelength of the X-ray source set in XRD, which is 0.154 nm, and b denotes the width of the peak of the diffraction at half maximum (FWHM) for the diffraction angle 2θ [23]. The mean crystallite sizes for CuO, LCoFO, CuO (40%)/LcoFO, CuO (60%)/LcoFO and CuO (70%)/LcoFO nanocomposites were found to be 94, 21.3, 40.72, 23 and 62.35 nm respectively.

The morphology and the particle size of the CuO (x)/LCoFO nanocomposites (x = 40, 60, and 70%) have been studied by SEM, and results are shown in figures 3 (a)- 3 (c), respectively.

CuO (60%)/LCoFO nanocomposite, compared to other nanocomposites with different CuO, the nanoparticles were linked to each other to create pores. Hence, the specific surface area (SSA) of the CuO (60%)/LCoFO nanocomposite is expected to increase with the increase of pores and the accumulation of particles [24, 25]. Moreover, we could predict that due to the lower accumulation of particles in CuO (40%)/LCoFO in comparison with CuO (60%)/LCoFO, there will be a decrease in the specific surface and surface pores. In addition, because of the greater accumulation of particles within the composites of CuO (x)/LCoFO with greater CuO content, 70% of the surface pores and their SSA are reduced. As a result, the PCA of the CuO (60%)/LCoFO composite was greater than the PCA of the other CuO (x)/LCoFO composites with 40, 70% CuO.

The morphologies of the LCoFO nanoparticles and CuO (60%)/LCoFO composite were studied using TEM images. These images show spherical particles like LCoFO and CuO (60%)/LCoFO. With an average grain size of 30 and 20 nm, respectively.

Figures 3 (e) and 3 (d) show that the irregular nanoparticles are formed by the aggregation of very small spheres. Nanoparticles with a higher density degree in the case of pure LCoFO compared to its CuO (60%)/LCoFO, which is identical due to the greater monodispersity of LCoFO.

Figure 4 (a) shows the FT-IR spectrum of LCoFO, CuO, and three CuO (x)/LCoFO (x = 40, 60, and 70%) nanocomposites, which contain varying amounts of CuO. In the spectrum of LCoFO, the peak at 570 cm^{-1} was related to the stretching vibration (SV) of Fe–O and the peak at around 420 was related to the bending vibration of O–Fe–O and [26]. As shown in the spectra, when there is an increase in the amount of CuO in the CuO (x)/LCoFO nanocomposites, there is a decrease in the peak intensity of Fe–O. The peaks at approxmately 1500 cm^{-1} were related to the existence of CO_3^{2-} achieved in the spectrum while preparing the FT-IR spectra in the air, whereas the peak at 2360 cm^{-1} demonstrates the SV and the bending vibration of the C=O bond of the O_2 adhered from the air [27, 28]. In the spectrum of CuO, the bands at 590, 526 cm^{-1} were indicative of the vibrational mode of Cu–O related to the SV band of the Fe–O in the CuO (x)/LCoFO composites [29].

In figure 4 (b), the curves exhibited broader absorption

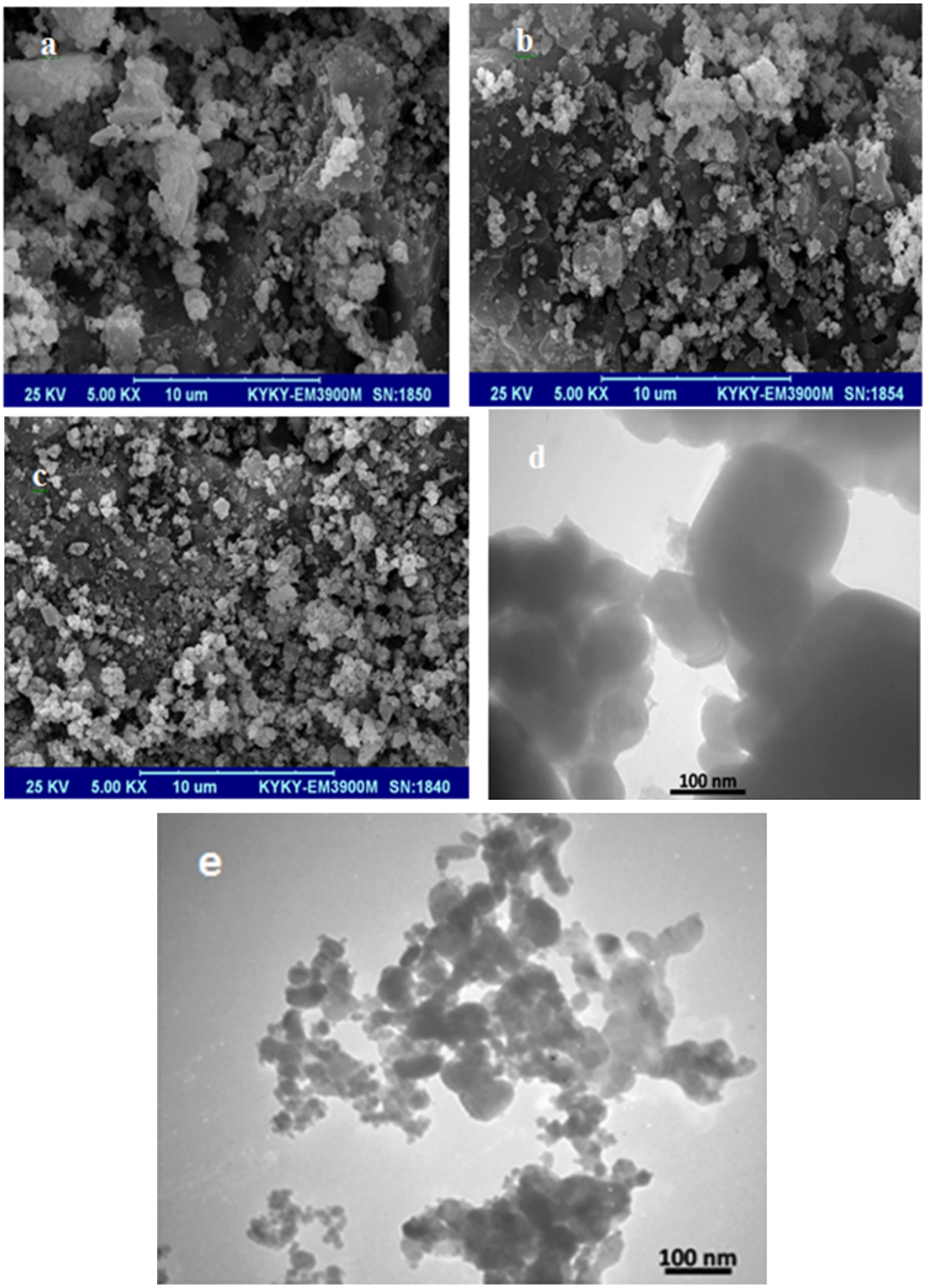

Figure 3. The (a-c) SEM micrographs for the CuO (x)/LCoFO (x = 40, 60, and 70%) composites. The TEM images of (d) LCoFO and (e) CuO (60%)/LCoFO composite.

bands in the U/V regions, indicating the capability of the CuO (x)/LCoFO (x = 40, 60, and 70%) in adsorbing a substantial amount of U/V light. Because CuO (x)/LCoFO (x = 40, 60, and 70%) nanocomposites show a stronger absorption peak than LCoFO and pure CuO, they should show higher photocatalytic activities.

Figure 5 (a) shows the magnetic properties of CuO (60%)/LCoFO nanocomposite photocatalyst. The coercion and saturation magnetization of this sample are about 137.53 Oe and 95.284 emu/g. The simultaneous presence of two ferromagnetic and paramagnetic properties in composite materials has been reported many times [30]. Based on published articles, ferromagnetic behavior can be attributed to the LCoFO sample and paramagnetic behavior to the CuO sample [31, 32].

Furthermore, when the CuO content in the composite increases, the Para magnetism property also increases gradually. Coexistence of ferromagnetism and paramagnetism

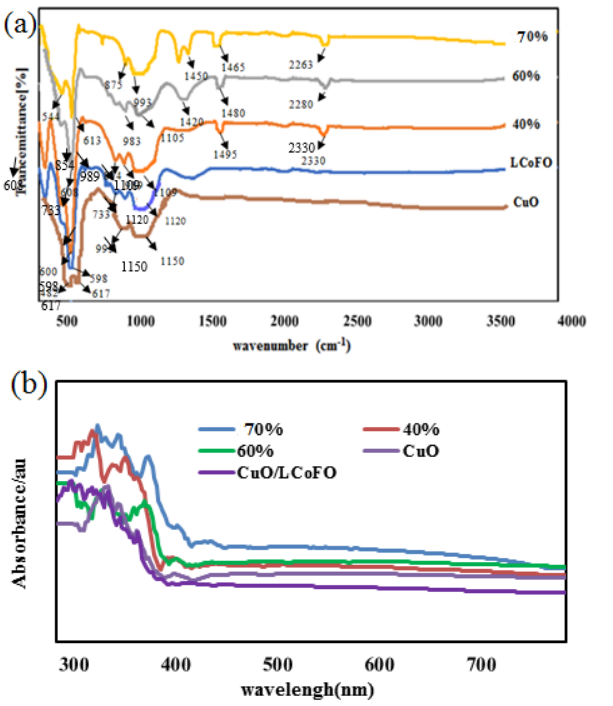

Figure 4. (a) FT-IR spectra of LCoFO, CuO and CuO (x)/LCoFO (x = 40, 60 and 70%) composites with different CuO contents. (b) The UV-Vis absorption CuO (x)/LCoFO (x = 40, 60and 100%) composites.

has been observed in some samples [30]. As the external magnetic field (H) increases, the sample behaves linearly (at fields higher than 5000 Oe). Therefore, the ferromagnetic sample does not enter the magnetic saturation state. But more carefully, we realize that this behavior is due to the nature of the presence of two samples with different magnetic properties in the composite sample: The LCoFO sample with ferromagnetic properties and the CuO sample with paramagnetic properties. For a quantitative and more detailed investigation, it is necessary to separate the magnetic contribution of these two materials from each other, and this can be seen in the figure 5 (b). on the other hand with increasing temperature, the magnetic susceptibility of diamagnetic minerals remains constant whereas that of paramagnetic minerals decreases according to the Curie-Weiss law The magnetic susceptibility of ferromagnetic minerals (in the broad sense) displays more complex variations. In a field of strength similar to the Earth's field, the ferromagnetic susceptibility increases gradually with increasing temperature up to the Curie temperature (Tc), and then it decreases abruptly [33].

To study the electrical, photoelectrical, and optical attributes of semiconducting nano-materials are used by pl spectroscopy. In figure 6, the PL spectrum of CuO (x)/LCoFO nanocomposites (x = 40, 60, and shows 70% with different amounts of CuO. Nanocomposites of CuO (x)/LCoFO (x = 40, 60, and 70%) show peaks in the wavelength range of 300 to 587 nm and have a sharp peak at about 587 nm. PL signals mostly because of the electronic transition from the conduction band to the valence band [34]. It goes without saying that when the PL peak is intense, the charge recombination rate is fast, and when the peak is broad, the electron-hole pairs will be separated more easily. As a re-

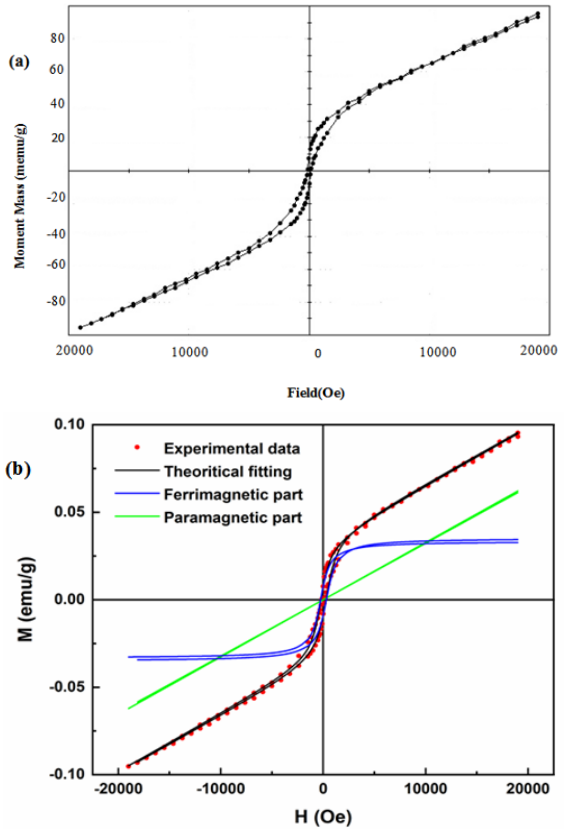

Figure 5. (a) Magnetization data of nanocomposite CuO (60%)/LCoFO and (b) simulated PM and b FM are shown for CuO (60%)/LCoFO.

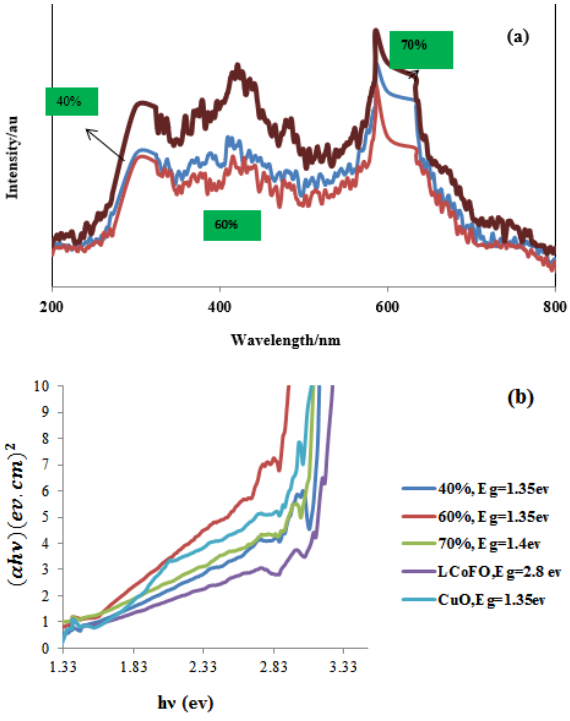

Figure 6. The (a) PL spectra of CuO (x)/LCoFO (x = 40, 60 and 100%) nanocomposites (b) the $(\alpha h\nu)^2$ versus $h\nu$ plots derived from the UV-Vis DRS spectra of pure $LaFeO_3$, CuO and three CuO (x)/$LaFeO_3$ (x = 40, 60, 70 and 70%) composites.

sult, the PL spectrum of the nanocomposite with 60% CuO shows the lowest PL intensity; therefore, the PCA of the sample is expected to increase by the highest separation of efficient electron-hole pairs.

Figure 6 (b) shows the plot of $(\alpha h\nu)^2$ versus $h\nu$ derived from the UV-Vis DRS spectra of pure $LaFeO_3$, CuO, and four CuO (x)/$LaFeO_3$ (x = 40, 50, 60 and 70%) composites which synthesized with different CuO contents The band gap energy can be determined by Eq. (3).

$$\alpha h\nu = A(h\nu - Eg)^{\frac{1}{2}} \tag{3}$$

For direct electron transfer, where A, Eg, and $h\nu$ are constants, the direct band gap energy and the incident photon energy, respectively. The band gap energy was estimated from the plot of $(\alpha h\nu)^2$ versus $h\nu$ by extrapolating the linear part $(\alpha h\nu)^2$ to zero. As shown in Fig. 4 (b), the optical band gaps of LCoFO and CuO are about 2.8 and 1.35 eV, respectively, which is close to what has been reported in the literature [35, 36].

3.2 Photocatalytic degradation study

3.2.1 Impact of CuO contents

The photocatalytic experiments are performed with an initial concentration of dye of 1.5 mg/L. Composites (x = 0 – 70%) and their PCA are compared. (figure 7 (a)). In this experiment, it can be seen that nanocomposites whose CuO content is less than 60% increase their photocatalytic activities. And in samples whose content is more than 60%, their PCA decreases. In explaining the cause of this case, it can be said that in nanocomposites with CuO above 60%, CuO particles are placed on the active sites in LCoFO, and this makes the PCA lower. The composites with a copper weight ratio to La 60:40 have the greatest decolorization efficiency amongst the other nanocomposites, as well as the ratios of pure LCoFO and pure CuO show. As seen in the articles [37]. CuO particles show extremely low PCA. CuO (60%)/LCoFO nanocomposite shows higher photocatalytic activity than LCoFO and CuO, which is probably due to the fact that the recombination of photo-generated electrons and holes in the pristine LCoFO as well as CuO was fast.

3.2.2 Effect of catalytic dosage

To find the optimal amount of the catalyst, experiments were conducted using different amounts of the optimal CuO (60%)/LCoFO photocatalyst from 1 to 7 g/L. There is a linear increase in the photocatalytic efficiency when the catalyst is loaded up to 7 g/L, and finally decreases and as shown in figure 7 (b). This behavior has been observed in other photocatalysts such as TiO_2, ZnO, $FeLaO_3$, $FeNdO_3$, and $LaCoFeO_3$. $La_2MnFe_2O_7$ and $La_2CuFe_2O_7$ [38–41]. When the photocatalyst active sites increase, the amounts of absorbed photons and the number of dye molecules increase, which improves the dye removal. On the other hand, with an increase in the amount of photocatalyst (more than

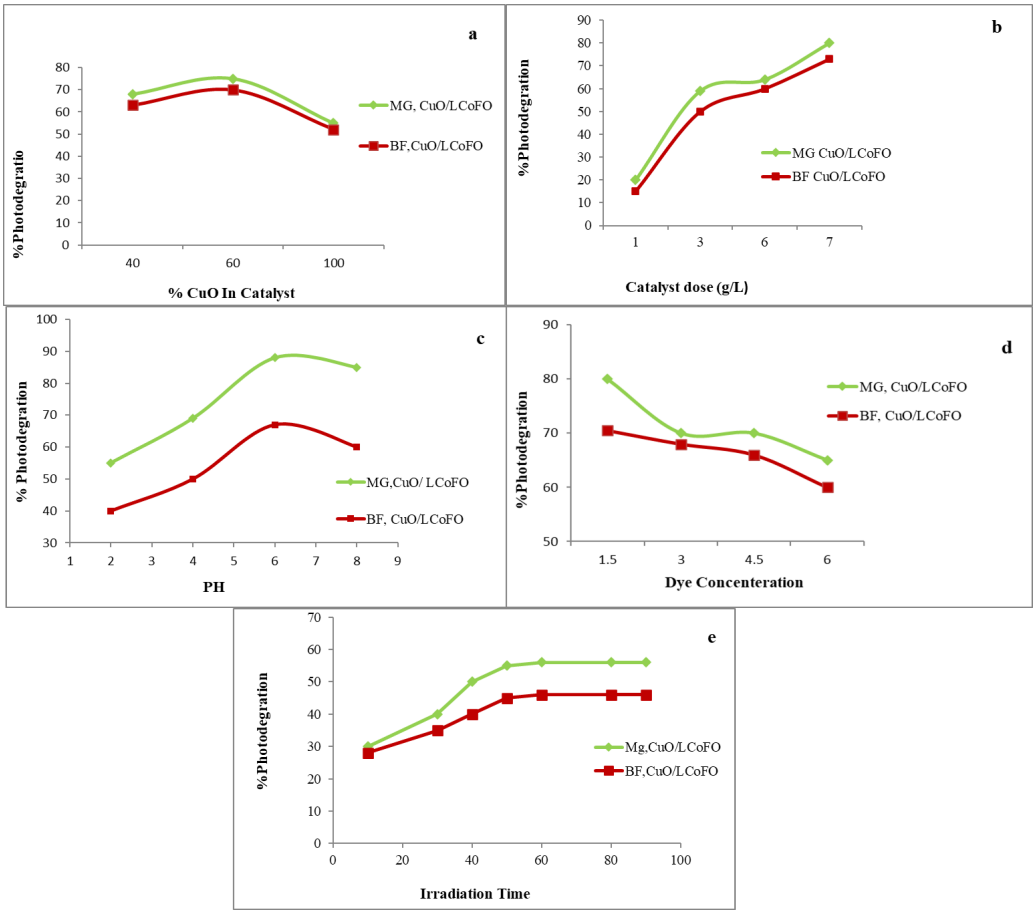

Figure 7. The Effects of (a) amount CuO, (b) catalyst dose, (c) pH, (d) dye concentration, (e) irradiation time on photodegradation of MG and FB by CuO (60%)/LCoFO nanocomposite and (e) photocatalysts .

7 g/L), probably due to condensation, the penetration of the irradiated light decreases and the scattering of the radiation increases, as a result, the active molecules become inactive and ultimately leads to a decrease in the decolorization efficiency [42]. Therefore, the optimal amount of photocatalysts was determined to be 7 g/L to increase the efficiency of the dye decomposition.

3.2.3 pH impact

Figure 7 (c) shows the impact of pH on the dye degradation efficiency. In investigating the effect of pH on color removal, the pH effect of 2.0 to 9.0 using CuO (60%)/LCoFO nanocomposite photocatalyst 7 g/L was investigated. In acidic and alkaline areas, the lowest color decomposition is observed, and in the neutral and slightly acidic range with pH (= 6), the highest efficiency of color decomposition is observed. Based on the zeta potential data, the charge level of the CuO (60%)/LCoFO composite was negative in alkaline pH and positive in acidic pH. The increase in the positive charge on the photocatalyst surface at very acidic pH results in the electrostatic repulsion between the cationic of MG and BF dye and the nano-photocatalyst, which reduces degradation also, at high pH, the active sites on the surface of the nanocatalyst and the color degradation are reduced when the adhesion of MG and BF is strong [43]. The findings obtained agree well with the zeta potential data.

3.2.4 Impact of the initial dye concentrations

Experiments were conducted to investigate the effect of the initial concentration of dye on the speed of dye removal. In these experiments, the initial concentration of dye was from 1.5 to 6 mg/L, and the amount of constant catalyst was 7 g/L, as shown in Fig. 7 (d). The rate of decolorization decreases with the increase of the initial concentration of the dye. This result is consistent with the studies of Napoleon and his colleagues [42]. In the process of dye degradation, one of the important species is OH radicals, which probably affects the rate of dye degradation. When the dye covers the active sites on the CuO (60%)/LCoFO nanocatalyst, there is a decrease in the number of photons and molecules that the nanocatalyst adsorbs. When the dye concentration is low, OH radicals at level CuO (60%)/LCoFO is formed, as a result of which OH radicals attack the dye molecules and absorb them. and as a result, the dye removal increases. However, at a high concentration of dye molecules, because the surface of the solution is covered by these molecules, as a result, the dye molecules adsorb most of the radiation, and the efficiency of dye decomposition decreases [49, 50].

3.2.5 Effect of irradiation time

Effect of irradiation time on photodegradation of MG and BF by CuO (x)/LCoFO nanoparticles and (7 g/L). The absorbers are shown in figure 7 (d). With the increase in Irradiation time up to 50 minutes, the photodegradation speed increased on nanoparticles. The biggest The amount of absorption occurred at 50 min and thereafter, further increase in time has no significant effect on photodeagration, occupied areas begin to repel absorbing molecules in the solution phase at the end times and in the case of adsorption of molecules, the available driving forces are weakened to reach the vacant surface areas, thus the absorption decreases [51]. Furthermore, the kinetics study, figure 8 (a), as inferred from the plot of $\ln(C/C_0)$ against time, demonstrates a rise in degradation over time, shown in figure 8 (a, b). This observation suggests the presence of a first-order

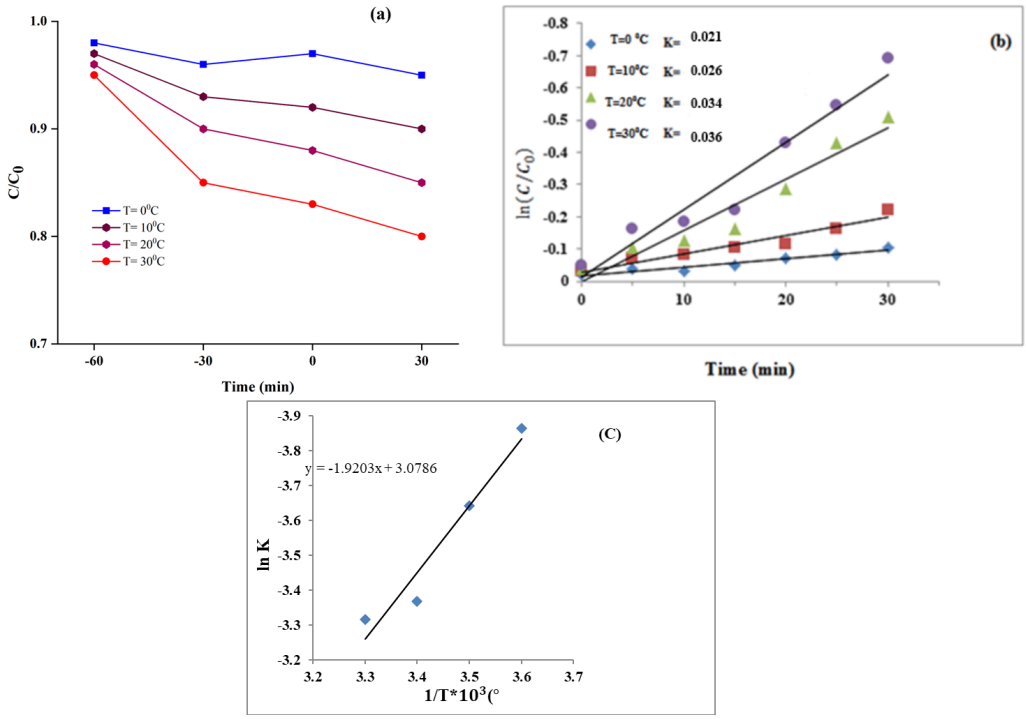

Figure 8. Plot of C/C_0 and $-\ln(C/C_0)$ for de colorization of MG dye of the prepared sample. (c) Arrhenius plot for the determination of *Ea* of degradation of MG dye at CuO(60%)/LcoFO.

degradation mechanism shown in Eq. (4)

$$\ln(\frac{C}{C_0}) = Kt \quad (4)$$

Comparison of the MG dye degradation rate constant at different pH shows that dye degradation at pH = 6 has the highest rate constant. The activation energy of MG degradation can be obtained using the linear form of the Arrhenius equation (5).

$$\ln k = \ln A - (\frac{Ea}{RT}) \quad (5)$$

The Arrhenius diagram of $\ln k$ was drawn in terms of $1/T$ and displayed in figure 8 (c). According to the curve slope, the activation energy of the MG photodegradation was estimated at 16 kJ/mol, which corresponds to the references [52].

3.3 Photodegradation mechanism

The process of the CuO/LCoFO photocatalytic reaction mechanism is shown in figure 9. As a result of UV light radiation, electron-hole pairs are created in the CuO/LCoFO nanoparticles (Eq. (1)). From the reaction of the hole created in VB with H_2O, the free radical $^{\bullet}OH$ is formed. This generated $^{\bullet}OH$ radical acts as a strong oxidizer and reacts with organic dye molecules adsorbed around the CuO/LCoFO nanophotocatalyst surface and oxidizes them, On the other hand, the electrons present in CB react with O_2, and in this reaction, superoxide radicals ($^{\bullet}O_2^-$) are produced. Superoxide radicals react with H^+ that are formed during the reaction. Protonated hydroproxyl radical ($^{\bullet}HO_2^-$), and finally hydroxyl radical ($^{\bullet}OH$) is produced. $^{\bullet}OH$ radicals react with dye molecules and create stable products. The reactions of this process are mentioned in Eqs. 2-9 [53]. PCA of CuO (60%)/LCoFO nanocomposite for degradation of organic dyes Methyl green and fuchsin, compared to several recent papers, are given in Table 1. CuO (60%)/LCoFO

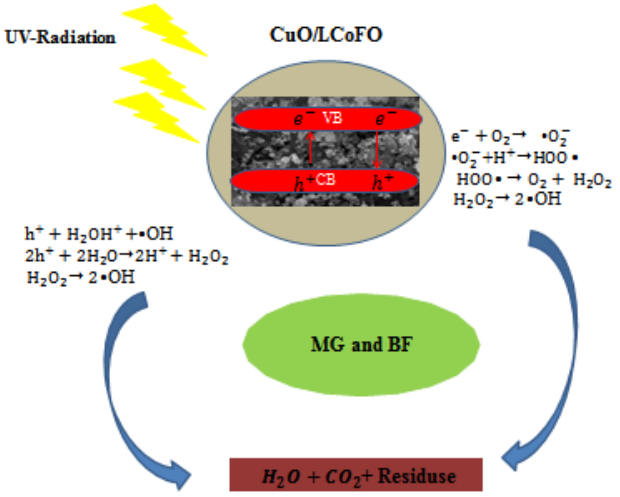

Figure 9. The photocatalytic mechanism of MG and BF on the CuO (60%)/LCoFO UV-light irradiation.

Nanocomposite has a good performance in the decomposition of organic dyes under UV light irradiation [9, 44–47]. The effect of $CoFe_2O_4$, La_2O_3, and CuO on color change was investigated, and the results were compared with those obtained from the synthesized composite in Table 2 [9, 48].

$$CuO/LCoFO + h\nu \rightarrow LaFeO_3/CuO\ (e^- + h^+) \quad (1)$$

$$h^+ + H_2O \rightarrow H^+ + OH^{\bullet} \quad (2)$$

$$2h^+ + 2H_2O \rightarrow 2H^+ + H_2O_2 \quad (3)$$

$$H_2O_2 \rightarrow 2OH^{\bullet} \quad (4)$$

Table 1. Degradation Performance Comparison of various catalysts photocatalyst for degradation of MG and BF.

No.	Catalysts	Target	Irradiation time (min)	Degration (%)	Ref.
1	$La_2CoFe_2O_7$	Malachite green	60	94	[14]
2	$Fe_3O_4/SiO_2/TiO_2$	Malachite green	150	100	[44]
3	Ce-B/TiO_2	Malachite green	120	90	[45]
4	GO/ZnO	Basic Fushin	300	92.5	[46]
5	Fe_3O_4	Basic Fushin	135	60	[46]
6	CuO/$La_2CoFe_2O_7$	Methyl green and Basic Fushin	50	99% MV, 98.8% BF	This work

Table 2. Degradation Performance Comparison of CuO, $CoFe_2O_4$, La_2O_3, and LCoFO on dye degradation.

No.	Catalysts	Target	Irradiation time (min)	Degration (%)	Ref.
1	$La_2CoFe_2O_7$	Malachite green	60	94	[14]
2	CuO	Rhodamine B	120	91	[47]
3	La_2O_3/Ag_3VO_4	Rhodamine B	90	90	[48]
4	CuO/$La_2CoFe_2O_7$	Methyl green and Basic Fushin	50	99% MV, 98.8% BF	This work

$$e^- + O_2 \rightarrow O_2^{\bullet -} \quad (5)$$

$$O_2^{\bullet -} + H^+ \rightarrow HOO^{\bullet} \quad (6)$$

$$HOO^{\bullet} \rightarrow O_2 + H_2O_2 \quad (7)$$

$$H_2O_2 \rightarrow 2OH^{\bullet} \quad (8)$$

$$Dye + OH^{\bullet} \rightarrow H_2O + CO_2 + Residues \quad (9)$$

4. Conclusion

The simple sol-gel method was employed to prepare the new CuO (x)/LCoFO nanocomposite photocatalysts (x = $0-70\%$) and the PCA of these samples was investigated using organic dye.

Results show the CuO (60%)/LCoFO nanocomposite photocatalyst has the highest PCA for color removal. This is due to the electron-hole separation caused by the electric field at the interface of these semiconductors, and it can also be because of the overlapping of the valence band and conductivity of the LCoFO and CuO surfaces. Because it increases the separation efficiency of the produced light. Therefore, it is concluded that the synthesized photocatalyst has special characteristics, such as being economical and non-toxic, and can be used in wastewater treatment.

Acknowledgment

We fully appreciate Payame Noor University for providing financial and technical support.

Authors contributions

Authors have contributed equally in preparing and writing the manuscript.

Availability of data and materials

The data that support the findings of this study are available from the corresponding author, upon reasonable request.

Conflict of interests

The author declare that they have no known competing financial interests or personal relationships that could have appeared to influence the work reported in this paper.

References

[1] S. Hussain, N. Farooq, A. S. Alkorbi, R. Alsaiari, N.A. Alhemiary, M. Wang, and G. Qiao. *J. Mole. Liq.*, **362**(2022):119765–119777. DOI: https://doi.org/10.1016/j.molliq.2022.119765.

[2] A. Nezamzadeh-Ejhieh and E. Shahriari. *Int. J. Photoenergy*, **2011**(2011):518153. DOI: https://doi.org/10.1155/2011/518153.

[3] A. Bakar Siddique, M. A. Shaheen, A. Abbas, Y. Zaman, M. A. Bratty, A. Najmi, A. Hanbashi, M. Mustaqeem, H.A. Alhazmi, Z.ur. Rehman, K. Zoghebi, M. A. Hatem, and H. M. A. Amin. *Heliyon*, **10**(2024):e40679. DOI: https://doi.org/10.1016/j.heliyon.2024.e40679.

[4] N. Assad, A. Abbas, M.F.ur. Rehman, and M. Naeem-ul Hassan. *RSC Adv*, **14**(2024):22344–22358. DOI: https://doi.org/10.1039/d4ra03573a.

[5] Z. Haider Ali, L. Abdulazeem, W. Alwan Kadhim, M. H. Kzar, and O. J. Al-sareji. *Sci. Rep.*, **14**(2024):31593. DOI: https://doi.org/10.1038/s41598-024-76090-w.

[6] B. Zohra, K. Aicha, S. Fatima, B. Nourredine, and D. Zoubir. *Che Eng J*, **136**(2008):295–305. DOI: https://doi.org/10.1016/j.cej.2007.03.086.

[7] J. Grzechulska and A. W. Morawski. *Appl. Catal. B Environ*, **36**(2002):45–51. DOI: https://doi.org/10.1016/S0926-3373(01)00275-2.

[8] F. Seidi and K. J. Hedayati. *Nanostruct*, **10**(2020):497–508. DOI: https://doi.org/10.22052/JNS.2020.03.006.

[9] A. A. Okab, Z. H. Jabbar, B. H. Graimed, and A. I. Alwared. *Nanomedicine & Nanotechnology Open Access (NNOA)*, **14**(2023): 1–13. DOI: https://doi.org/10.23880/nnoa-16000272.

[10] Q. Zhou, Z. Fang, J. Li, and M. Wang. *Micropor. Mesopor. Mater.*, **202**(2015):22–35, . DOI: https://doi.org/10.1016/j.micromeso.2014.09.040.

[11] H. Tian, J. Ma, K. Li, and J. Li. *Ceram. Int.*, **35**(2009):1289–1292. DOI: https://doi.org/10.1016/j.ceramint.2008.05.003.

[12] H. Yang, K. Zhang, R. Shi, X. Li, X. Dong, and Y. Yu. *J. Alloy. Compd.*, **413**(2006):302–306, . DOI: https://doi.org/10.1016/j.jallcom.2005.06.061.

[13] A. Yousefi and A. Nezamzadeh-Ejhieh. *Iran. J. Catal.*, **11**(2021): 247–259. URL http://oiccpress.com/ijc/article/view/3600.

[14] S. Khammarnia, J. Saffari, and M.-S. Ekrami-Kakhki. *Journal of Color Science and Technology (JCST)*, **17**(2023):245–255, . DOI: https://doi.org/20.1001.1.17358779.1402.17.3.5.8.

[15] K. Varaprasad, K. Ramam, G. S. M. Reddy, and R. Sadiku. *RSC Adv.*, **4**(2014):60363–60370. DOI: https://doi.org/10.1039/C4RA09980J.

[16] J. Zhu, H. Li, L. Zhong, P. Xiao, X. Xu, X. Yang, Z. Zhao, and J. Li. *ACS Catal.*, **4**(2014):2917–2940. DOI: https://doi.org/10.1021/cs500606g.

[17] Q. Yu, X. Meng, T. Wang, P. Li, L. Liu, K. Chang, G. Liu, and J. Ye. *Chem. Commun.*, **51**(2015):3630–3633. DOI: https://doi.org/10.1039/C4CC09240F.

[18] Y. Qu, W. Zhou, Y. Xie, L. Jiang, J. Wang, G. Tian, Z. Ren, C. Tian, and H. Fu. *Chem. Commun.*, **49**(2013):8510–8512. DOI: https://doi.org/10.1039/C3CC43435D.

[19] J. Yang, R. Hu, W. Meng, and Y. Du. *Chem. Commun.*, **52**(2016): 2620–2623, . DOI: https://doi.org/10.1036/C5CC09222A.

[20] K. Zhou, R. Wang, B. Xu, and Y. Li. *Nanotechnology*, **17**(2006): 3939–3943, . DOI: https://doi.org/10.1088/0957-4484/17/15/055.

[21] Y. Soltanabadi, M. Jourshabani, and Z. Shariatinia. *Separation and Purification Technology*, **202**(2018):227–241. DOI: https://doi.org/10.1016/j.seppur.2018.03.019.

[22] S. Sharafzadeh, J. Zolgharnein, A. Nezamzadeh–Ejhieh, and S. Dermanaki Farahani. *Surf. Interfaces.*, **59**(2025):105917, . DOI: https://doi.org/10.1016/j.surfin.2025.105917.

[23] M. K. Satheeshkumar, E. Ranjith Kumar, C. Srinivas, G. Prasad, S. S. Meena, I. Pradeep, N. Suriyanarayanan, and D. L. Sastry. *J. Magn. Magn. Mater*, **484**(2019):120125. DOI: https://doi.org/10.1016/j.jmmm.2019.03.128.

[24] W. Li, H. Shen, and J. Xu. *J. Sol-Gel Sci. Technol.*, **76**(2015): 637–643, . DOI: https://doi.org/10.1007/s10971-015-3815-0.

[25] J. Wang J. Zhou K. Wu Y. Cheng W. Fan, Z. Sun. *J. Power Sourc.*, **312**(2016):223–233.
DOI: https://doi.org/10.1016/j.jpowsour.2016.02.069.

[26] T. Yosuke, S. Hiromi, and N. Kazuya. *Mater.Res. Bull.*, **41**(2006): 834–841.
DOI: https://doi.org/10.1016/j.materresbull.2005.10.004.

[27] M. Vaseem, A. Umar, S. H. Kim, and Y.-B. Hahn. *J. Phys. Chem. C*, **112**(2008):5729–5735.
DOI: https://doi.org/10.1021/jp710358j.

[28] L. Hou, G. Sun, K. Liu, Y. Li, and F. Gao. *Preparation, J. Sol-Gel Sci. Technol.*, **40**(2006):9–14.
DOI: https://doi.org/10.1007/s10971-006-8368-9.

[29] G. Kliche and Z. V. Popovic. *Phys. Rev. B*, **42**(1990):10060–10066.
DOI: https://doi.org/10.1103/PhysRevB.42.10060.

[30] W. Wang, L. Xu, R. Zhang, J. Xu, F. Xian, J. Su, and F.Yang. *Chem. Phys. Lett.*, **721**(2019):57–61, .
DOI: https://doi.org/10.1016/j.cplett.2019.02.031.

[31] A. A. Samokhvalov, T. I. Arbusova, N. A. Viglin, S. V. Naumov, V. R. Galakhov, D. A. Zatsepin, Yu. A. Kotov, O. M. Samatov, and D. G. Kleshchev. *Physics of the Solid State*, **40**(1998):268–271.
DOI: https://doi.org/10.1134/1.1130290.

[32] W. Wang, W. Feng, J. Yuan, N. Pang, X. Zhao, M. Li, Z. Bao, K. Zhu, and D. Odkhuu. *Physica B: Condensed Matter*, **540**(2018):33–37, .
DOI: https://doi.org/10.1016/j.physb.2018.04.018.

[33] F. Martı ̀n-Hernández and E.C. Ferre. *J. Geophys. Res.*, **112**(2007): B03105.
DOI: https://doi.org/10.1029/2006JB004340.

[34] S. Li, L. Jing, W. Fu, L. Yang, B. Xin, and H. Fu. *Mater. Res. Bull.*, **42**(2007):203–212, .
DOI: https://doi.org/10.1016/j.materresbull.2006.06.010.

[35] P. Ma, W. Jiang, F. Wang, F. Li, P. Shen, M. Chen, Y. Wang, J. Liu, and P. Li. *J. Alloy Compd.*, **578**(2013):501–506.
DOI: https://doi.org/10.1016/j.jallcom.2013.07.026.

[36] Q. Zhou, Z. Fang, J. Li, and M. Wang. *Micropor. Mesopor. Mater.*, **202**(2015):22–35, .
DOI: https://doi.org/10.1016/j.micromeso.2014.09.040.

[37] R. Gusain, P. Kumar, O. P. Sharma, S. L. Jain, and O. P. Khatri. *Appl. Catal. B Environ.*, **181**(2016):352–362.
DOI: https://doi.org/10.1016/j.apcatb.2015.08.012.

[38] S. Khammarnia, J. Saffari, and M. S. Ekrami-Kakhki. *Chem Rev Lett*, **7**(2024):123–133, .
DOI: https://doi.org/10.22034/CRL.2024.434922.1277.

[39] S. Khammarnia, A. Akbari, J. Saffari, and M.-S. Ekrami-Kakhki. *J. Clust. Sci.*, **30**(2019):1383–1391, .
DOI: https://doi.org/10.1007/s10876-019-01580-1.

[40] M. H. Habibi, A. Hassanzadeh, S. Mahdavi, and J. Photochem Photobiol. *A Chem.*, **172**(2005):89–96.
DOI: https://doi.org/10.1016/j.jphotochem.2004.11.009.

[41] A. Akyol and M. Bayramoğlu. *J. Hazard. Mater.*, **124**(2005):241–246.
DOI: https://doi.org/10.1016/j.jhazmat.2005.05.006.

[42] B. Neppolian, M. V. Shankar, and V. Murugesan. *Semiconductor assisted photodegradation of textile dye*, (2002). ISSN 0975-1084.

[43] E. Bizani, K. Fytianos, I. Poulios, and V. Tsiridis. *J.Hazard. Mater.*, **136**(2006):85–94.
DOI: https://doi.org/10.1016/j.jhazmat.2005.11.017.

[44] S. Gita, S. P. Shukla, G. Deshmukhe, T. G. Choudhury, N. Saharan, and A. K. Singh. *Bull. Environ. Contam. Toxicol.*, **106**(2021):302–309.
DOI: https://doi.org/10.1007/s00128-020-03074-7.

[45] M. Farhadian and M. Kazemzad. *Synth. React. Synth. React. Inorg. M.*, **46**(2016):458–463.
DOI: https://doi.org/10.1080/15533174.2014.988802.

[46] M. Shariati, A. Babaei, and A. Azizi. *J. Mater. Res.*, **38**(2023):2666–2678.
DOI: https://doi.org/10.1557/s43578-023-00990-2.

[47] M. Jeevarathinam and I. V. Asharani. *Sci. Rep.*, **9718**(2024):9718.
DOI: https://doi.org/10.1038/s41598-024-60008-7.

[48] M. Mylarappa, C. Selvam, K. Harisha, H. K. Sanjeevappa, S. G. P. Prasanna Kumar, G. Krishnamurthy, and N. Kalasad Muttanagoud. *Results in Surfaces and Interfaces*, **14**(2024):100202.
DOI: https://doi.org/10.1016/j.rsurfi.2024.100202.

[49] A. P. Toor, A. Verma, C. K. Jotshi, P. K. Bajpai, and V. Singh. *Dye. Pigment.*, **68**(2006):53–60.
DOI: https://doi.org/10.1016/j.dyepig.2004.12.009.

[50] I. K. Konstantinou and T. A. Albanis. *Appl. Catal. B Environ.*, **49**(2004):1–14.
DOI: https://doi.org/10.1016/j.apcatb.2003.11.010.

[51] R. Ahmad. *J Hazard Mater*, **171**(2009):767–773.
DOI: https://doi.org/10.1016/j.jhazmat.2009.06.060.

[52] S. Sharafzadeh, J. Zolgharnein, A. Nezamzadeh–Ejhieh, and S. Dermanaki Farahani. *Int. J. Hydrogen Energy*, **106**(2025):1429–1442, .
DOI: https://doi.org/10.1016/j.ijhydene.2025.02.031.

[53] G. Mishra and M. Mukhopadhyay. *Sci. Rep.*, **9**(2019):4345.
DOI: https://doi.org/10.1038/s41598-019-40775-4.